**ROYAL SOCIETY OF CHEMISTRY**

Check for updates

# Investigation of temperature and frequency dependence of the dielectric properties of multiferroic (La$_{0.8}$Ca$_{0.2}$)$_{0.4}$Bi$_{0.6}$FeO$_3$ nanoparticles for energy storage application

Amira Bougoffa, [ID] *[a] E. M. Benali, [ID] [ad] A. Benali,[abd] M. Bejar, [ID] [a] E. Dhahri, [ID] [a] M. P. F. Graça, [ID] [b] M. A. Valente, [ID] [b] G. Otero-Irurueta[c] and B. F. O. Costa[d]

In this work we synthesized the multifunctional (La$_{0.8}$Ca$_{0.2}$)$_{0.4}$Bi$_{0.6}$FeO$_3$ material using a sol–gel process. Structural and morphologic investigations reveal a *Pnma* perovskite structure at room temperature with spherical and polygonal nanoparticles. A detailed study of the temperature dependence of the dielectric and electrical properties of the studied material proves a typical FE–PE transition with a colossal value of real permittivity at 350 K that allows the use of this material in energy storage devices. Thus, the investigation of the frequency dependence of the ac conductivity proves a correlated barrier hopping (CBH) conduction mechanism to be dominant in the temperature ranges of 150–170 K; the two observed Jonscher's power law exponents, $s_1$ and $s_2$ between 180 K and 270 K correspond to the observed dispersions in the ac conductivity spectra in this temperature region, unlike in the temperature range of 250–320 K, the small polaron tunnel (NSPT) was considered the appropriate conduction model.

## 1. Introduction

The evolution of human activities, the increase of world population and the integration of new technologies has led to a strong growth in energy needs. Therefore, the increase of this consumption can result the depletion of the materials for energy production. It is then expected that the price of these materials will further increase which makes academia and industry research new efficient materials with low cost and simple synthesis processes.

Recently, great attention is granted to multiferroic materials due to the diversity of their application fields due to the combination of their ferroelectric and ferromagnetic behavior and their dependence on both frequency and temperature.[1]

Therefore, these materials can provide simultaneously different solutions to energy production problems. Indeed, perovskite structured LaFeO$_3$ has been intensively studied because of its particular properties making it a potential material for several applications: chemical sensors,[2] catalytic devices,[3] fuel cells,[4] gas sensors,[5] memory devices and magnetic refrigerants.[6] This typical material exhibited a high ferroelectric

transition temperature ($\approx$715 K).[7] In order to shift this transition near the room temperature and enhance the dielectric stability, a significant number of researches have been developed a diversity of substitutions at A or/and B-sites of these materials.[8] In fact, introducing another cation in the A or B site can perturb the neutrality of the perovskite structure resulting then a strong change on the structural and physical properties.[9–12] Previous research works, reported that bismuth atom exhibits golden properties where its introduction in perovskite materials can induce multiferroic properties.[13] This kind of materials can provide several dielectric behaviors at the same time (ferroelectric, anti-ferroelectric, ferromagnetic…). As it is well known, in these days, anti-ferroelectrics, ferroelectrics, linear dielectrics, and relaxor ferroelectrics materials present the frequent dielectric materials for electronic devices applications.[14] By comparing with linear dielectric and ferroelectric materials, anti-ferroelectrics ones exhibit generally a significantly high energy-storage density due to the absence of remnant polarization ($P_r$).[15] In another hand, relaxor ferroelectrics behave efficient because of their low $P_r$ value that is why they are frequently requested as an ideal ceramic for energy-storage applications.[16,17]

Therefore, the aim of this study is to investigate the temperature and frequency dependence of dielectric properties of the multiferroic (La$_{0.8}$Ca$_{0.2}$)$_{0.4}$Bi$_{0.6}$FeO$_3$ compound. In fact, the studied material was prepared by sol–gel route. Then, the X-ray diffraction was used to examine the purity and the crystal structure. The morphology and particles size have been

[a]*Laboratory of Applied Physics, Faculty of Sciences of Sfax, University of Sfax, B. P. 1171, Sfax, 3000, Tunisia. E-mail: amirabougoffa@gmail.com; Tel: +216 26 923 772*
[b]*I3N, Physics Department, University of Aveiro, Campus de Santiago, Aveiro, Portugal*
[c]*Centre for Mechanical Technology& Automation (TEMA), University of Aveiro, 3810-193, Aveiro, Portugal*
[d]*University of Coimbra, CFisUC, Physics Department, Rua Larga, P-3004-516 Coimbra, Portugal*

observed by electron scanning microscopy and the Transmission Electronic Microscopy (TEM). Thus, the XPS technique aims to study and quantify the oxidation state of the chemical elements that constitute the studied compound. The dielectric measurements were performed under the temperature range 150–400 K and the frequency range of $10^2$–$10^6$ Hz in order to discuss the temperature and frequency dependence of the electrical and dielectric properties of the prepared material.

## 2. Preparation methods

### 2.1 Sol–gel route

$(La_{0.8}Ca_{0.2})_{0.4}Bi_{0.6}FeO_3$ nanosize compound was prepared by the sol–gel method using the citric acid route.[18,19] Stoichiometric amounts of high-purity lanthanum nitrate $(La(NO_3)_3 \cdot 6H_2O)$, iron(III) nitrate nonahydrate $(Fe(NO_3)_3 \cdot 9H_2O)$, calcium nitrate $(Ca(NO_3)_2 \cdot 4H_2O)$ and bismuth nitrate pentahydrate $(Bi(NO_3)_3 \cdot 9H_2O)$ were dissolved in ethylene glycol in proper stoichiometric proportions. The mixture solution was stirred continuously until a clear solution was observed. Then, an appropriate amount of citric acid (molar ration nitrates/citric acid equal to 1/2) was added to the solution and magnetic stirred for almost 2 hours at 70 °C until a viscous gel was formed. The formed gel was heated at 170 °C with continuous stirring which promotes the evaporation of gases and the formation of a brown residue powder which was heated at 300 °C for 12 hours. After that the obtained powder was grounded and pressed into pellets with 7 mm of diameter, under an axial pressure of about $10^4$ N cm$^{-2}$, and then annealed 4 hours at 800 °C to finally obtain the $(La_{0.8}Ca_{0.2})_{0.4}Bi_{0.6}FeO_3$ compound.

### 2.2 Characterization methods

The phase and structure of the as-prepared powder were determined by X-Ray Diffraction (XRD) using the Bruker D8 Advance X-ray powder diffractometer with CuK$_{\alpha 1}$ radiation ($\lambda = 1.5406$ Å). After that the, the obtained pattern was refined using the FullProf software[20] in order to extract the lattice parameters and the structural positions of atoms. Microstructures and grain sizes were evaluated by a TESCAN VEGA3 SBH microscope, operating at 20 kV and equipped with an EDS detector BRUKERXFLAGH 410M, which allowed the detection of the characteristic X-rays emitted by the sample and, thus, the identification of its chemical elements. TEM images were obtained with a FEI Tecnai G2 with an acceleration voltage of 200 kV, in bright field. The carbon grids were immersed in dilute suspensions of the nanoparticles and, after sonication the grids were placed in the microscope. ImageJ software was used to obtain the size of the nanocomplexes.

The XPS spectra were acquired in an Ultra High Vacuum (UHV) system with a base pressure of $2 \times 10^{-10}$ mbar. The system is equipped with a hemispherical electron energy analyzer (SPECS Phoibos 150), a delay-line detector and a monochromatic AlK$\alpha$ (1486.74 eV) X-ray source. High resolution spectra were recorded at normal emission take-off angle and with a pass-energy of 20 eV, providing an overall

instrumental peak broadening of 0.5 eV. The resulting XPS spectra were calibrated in binding energy and using the C 1s peak as a reference from contamination at 285.0 eV.

For the dielectric measurements, the sample was kept in a helium atmosphere to minimize thermal gradient. An Oxford Research IT-C4 was equipped to control the temperature that was measured using a platinum sensor under the range from 150 K to 400 K. Then, the impedance of the sample was measured with an Agilent 4294 Network Analyzer in the frequency range between 100 Hz and 1 MHz in the $C_p$–$R_p$ configuration (capacitance in parallel with resistance).[21–23]

## 3. Results and discussions

### 3.1 Structural study

We plotted in Fig. 1(a) the room temperature X-ray diffractogram of the $(La_{0.8}Ca_{0.2})_{0.4}Bi_{0.6}FeO_3$ compound. As we can see, eight characteristic peaks at $2\theta$ equal to 22.65°, 32.24°, 39.75°, 46.22°, 52.08°, 57.47°, 67.40°, and 72.68° have been detected. These diffractions peaks correspond well respectively to the (110), (121), (220), (202), (141), (240), (242), and (024) planes of the layered structure of lanthanum ferrite LaFeO$_3$ (JCPDS card No. 96-152-6451),[24] as presented in Fig. 1(b). The XRD pattern of the $(La_{0.8}Ca_{0.2})_{0.4}Bi_{0.6}FeO_3$ compound found to be almost identical to that of previously studied La$_{0.8}$Ca$_{0.2}$FeO$_3$ studied compound[25] with a slight modification of the peak positions following the insertion of Bi$^{3+}$ ions in A-site. Importantly, we mention that for BiFeO$_3$ multiferroic material, the insertion of 20% of lanthanum ions in A-site leads to a structural transition from rhombohedral ($R3c$) to orthorhombic ($Pnma$).[26] Additionally, some other diffraction peaks with a very low intensity have been detected and were associated to the Bi$_2$Fe$_4$O$_9$ minoritarian phase according to the X-pert High score software. The



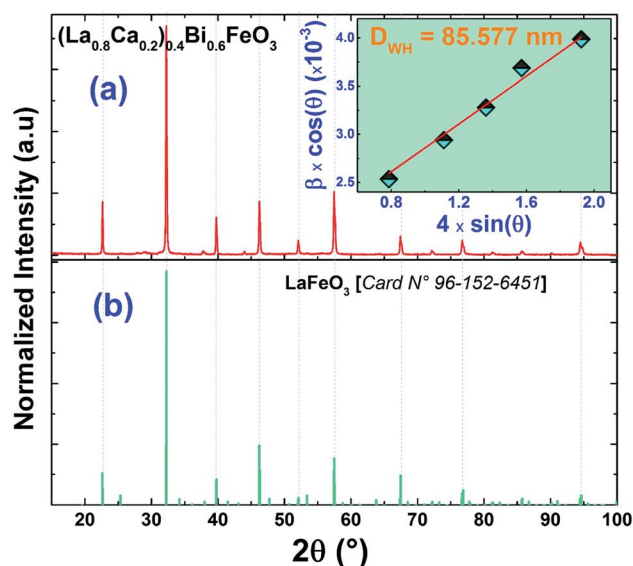**Fig. 1** XRD patterns of the (a) $(La_{0.8}Ca_{0.2})_{0.4}Bi_{0.6}FeO_3$ compound and (b) the standard data of LaFeO$_3$ (JCPDS No.96-152-6451). The inset of (a) presents the Williamson–Hall plot of the $(La_{0.8}Ca_{0.2})_{0.4}Bi_{0.6}FeO_3$ compound.

appearance of the secondary $Bi_2Fe_4O_9$ phase is in good agreement with previous studies.[27–29] We have also calculated the average crystallite size ($D_{WH}$) using the position and the half width of the five most intensive peaks according to the Williamson–Hall formalism[30] (eqn (1)).

$$\beta_{hkl} \cos(\theta) = \frac{0.9 \times \lambda}{D_{W-H}} + 4 \times \varepsilon \times \sin(\theta) \tag{1}$$

where $D_{W-H}$ is the average crystallite size, $\lambda$ (1.5405 Å) represents the used wavelength, $\theta$ is the Bragg angle of the most intense peak, $\beta$ is the full-width at half maximum (FWHM) and $\varepsilon$ is the effective strain. The Williamson–Hall curve is presented in the inset of Fig. 1(a) and as we can see, the average crystallite size is around 85.557 nm, which confirms well the nanosize criteria of the studied compound.

Furthermore, in order to have deep information about the insertion of 60% of $Bi^{3+}$ ions in A-site on structural properties we have adjusted the XRD pattern according to the Rietveld refinement method using the FULLPROF Rietveld software[20] and the refinement results of the XRD patterns for both compounds are plotted in Fig. 2. As one can see, the refinement has been realized with a majoritarian *Pbnm* phase and a second *Pbma* associated to the mean phase and the secondary phase, respectively. In this figure, the black color refer to the experimental diffractogram, the blue one present to calculated spectrum, the difference between the two in displayed in red color and the Bragg positions are shown in green. The resulting lattice parameters and the volume values are presented in Fig. 2.

We note here that the parameter $\chi^2$ informs us about the quality of the fit. It is an agreement between the observed and calculated diffractogram, close to unity for perfect refinement.

## 3.2 Morphological

We have used a Scanning Electron Microscope (SEM) in order to analyze the surface morphology of the $(La_{0.8}Ca_{0.2})_{0.4}Bi_{0.6}FeO_3$ compound. As one can see in Fig. 3, SEM image shows a high dense morphology of grains with spherical and polygonal shapes. The EDS spectra and the EDX area mapping are shown also in Fig. 3(a–g). Accordingly, we confirm that all chemical elements are present and are homogeneously distributed in the $(La_{0.8}Ca_{0.2})_{0.4}Bi_{0.6}FeO_3$ compound which confirms no loss of any chemical element during the preparation steps.

For further analyses of the particle size in the prepared compound, the "Image-J" software has been used to estimate the average particle size ($D_{TEM}$) from TEM image for $(La_{0.8}Ca_{0.2})_{0.4}Bi_{0.6}FeO_3$ compound as shown in Fig. 3(h) and (i). Note that the average particle size was determined by a Lorentzian fit of the particle size distribution deduced from the Image-J result. The average particle size $D_{TEM}$ of the studied compound was found to be around 88.73 nm. This value is almost equal to the average crystallite sized $D_{WH}$ calculated by the Williamson–Hall method indicating that each grain is made up of one crystallite. Importantly, we confirm the nanosize criteria of the $(La_{0.8}Ca_{0.2})_{0.4}Bi_{0.6}FeO_3$ compound.

## 3.3 XPS study

The X-ray Photoemission Spectroscopy (XPS) was employed to analyze the electronic structure of the $(La_{0.8}Ca_{0.2})_{0.4}Bi_{0.6}FeO_3$ material.

As displayed in Fig. 4, all the peak positions were indexed referring to the National Institute of Standards and Technology (NIST) XPS database.[31] The survey scan reveals the presence of the constituent elements: La, Ca, Bi, Fe, and O as well as the absence of any foreign element in this compound other than C 1s one located at about 285.0 eV. Indeed, the presence of this element can be due to the surface adsorbed C atoms from the atmosphere which occurs quite commonly in the XPS spectra of many compounds.

Fe 2p core level shown in Fig. 4(a) can be deconvoluted by two set of components ascribed to $Fe^{2+}$ (blue components) and $Fe^{3+}$ (green). Previous works on similar samples indicated that a slight oxygen deficiency results in the combination of $Fe^{2+}$ and $Fe^{3+}$ ions.[32,33] The ratio $Fe^{3+}/Fe^{2+}$ obtained by the fit of the XPS spectra was 1.2, slightly higher than the recently obtained by Zhang *et al.* for BFO samples.[30] $Fe^{2+}$ components were centred at binding energies (BEs) of 709.6 eV, 715 eV, 722.8 eV and 728.2 eV and they were ascribed to Fe $2p_{3/2}$, a satellite, Fe $2p_{1/2}$ and a satellite, respectively. Similarly, the respective components ascribed to $Fe^{3+}$ appeared at BEs of 711.5 eV (Fe $2p_{3/2}$), 718.9 eV (sat.), 724.8 eV (Fe $2p_{1/2}$) and 731.8 eV (sat.). These values are in good agreement with previous reported values for Fe 2p core level.[32,34,35] On the other hand, O 1s (Fig. 4(b)) was fitted by two components centred at BEs of 529.9 eV and 532.1 eV. The component at lower BE was ascribed to the oxygen atoms in the lattice while the other is associated to hydroxyl groups covering the surface structural defects (oxygen vacancies).[32] Moreover, as shown in Fig. 4(c), Bi 4f was fitted by two components at BEs of 158.7 eV and 164.0 eV. The component at lower BE is ascribed to Bi $4f_{7/2}$ while the component at higher BE is Bi $4f_{5/2}$. Both, the energies of the peaks and the spin–orbit splitting between them (5.3 eV) are in good agreement with oxidized bismuth ($Bi^{3+}$).[32–34,36]



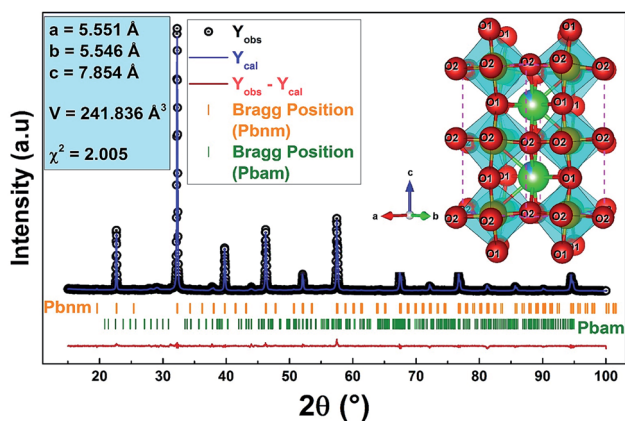**Fig. 2** The XRD Rietveld refinement results of the $(La_{0.8}Ca_{0.2})_{0.4}Bi_{0.6}FeO_3$ compound. The inset of the figure presents generated crystal structure and representation of $FeO_6$ polyhedron of the studied compound.
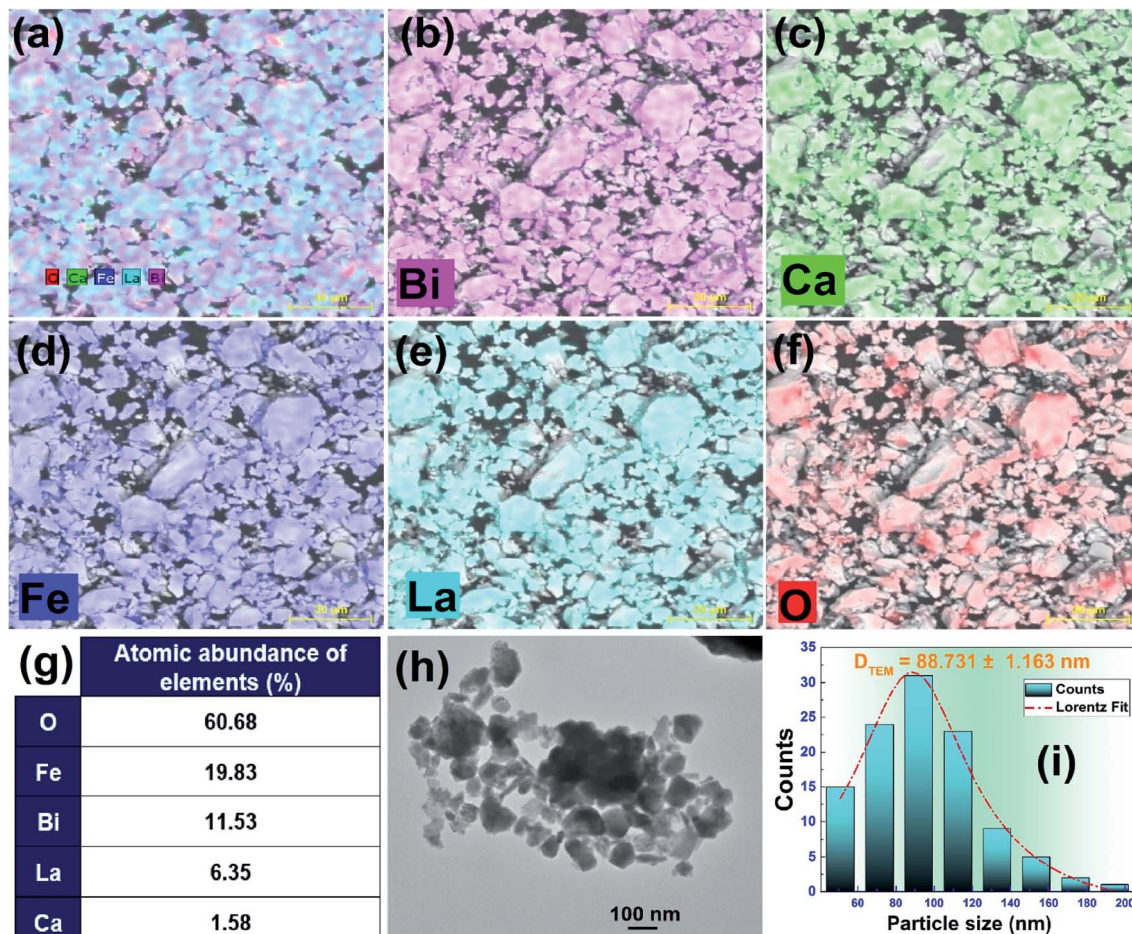
Fig. 3 (a–f) Elemental mapping of La, Ca, Bi, Fe, and oxygen; (g) EDX spectra; (h) TEM micrograph and (i) the corresponding size distribution analysis of the $(La_{0.8}Ca_{0.2})_{0.4}Bi_{0.6}FeO_3$ compound.

## 3.4 Dielectric properties

**3.4.1 Temperature dependence of dielectric behavior.** Fig. 5(a) proves the variation of the real dielectric permittivity ($\varepsilon'$) of the $(La_{0.8}Ca_{0.2})_{0.4}Bi_{0.6}FeO_3$ material *versus* temperature under the frequency range from $10^2$ Hz to $10^6$ Hz. It is clear that this compound presents four dielectric anomalies observed at: 180 K, 240 K, 320 K and 350 K. As demonstrated by Fig. 5(b), the plot of $d\varepsilon'/dT$ as a function of temperature can clearly confirm these transitions. In the other hand, Fig. 5(c) displays the variation of the imaginary part of the dielectric permittivity ($\varepsilon''$) of
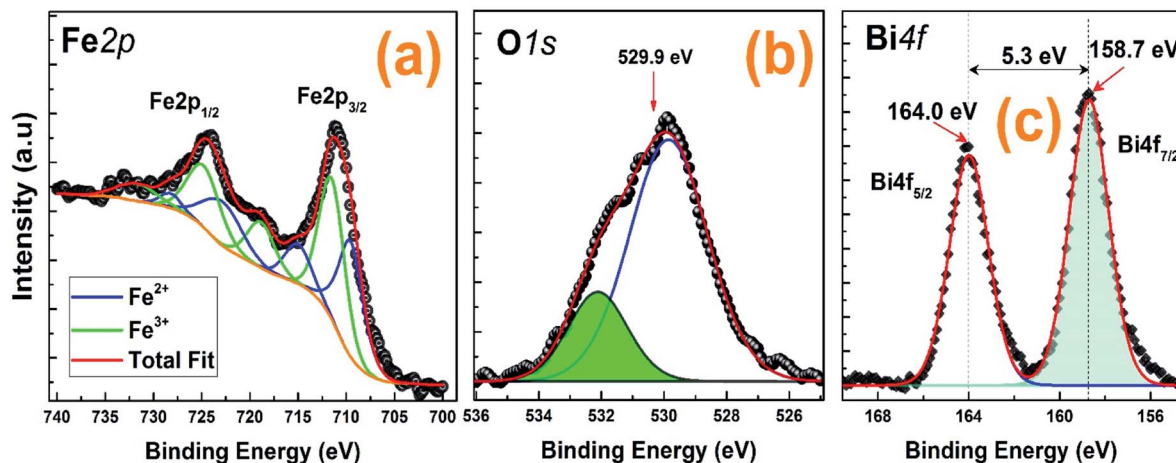


Fig. 4 XPS results obtained of (a) Fe 2p, (b) O 1s and (c) Bi 4f for the $(La_{0.8}Ca_{0.2})_{0.4}Bi_{0.6}FeO_3$ compound. The best fits are also included.
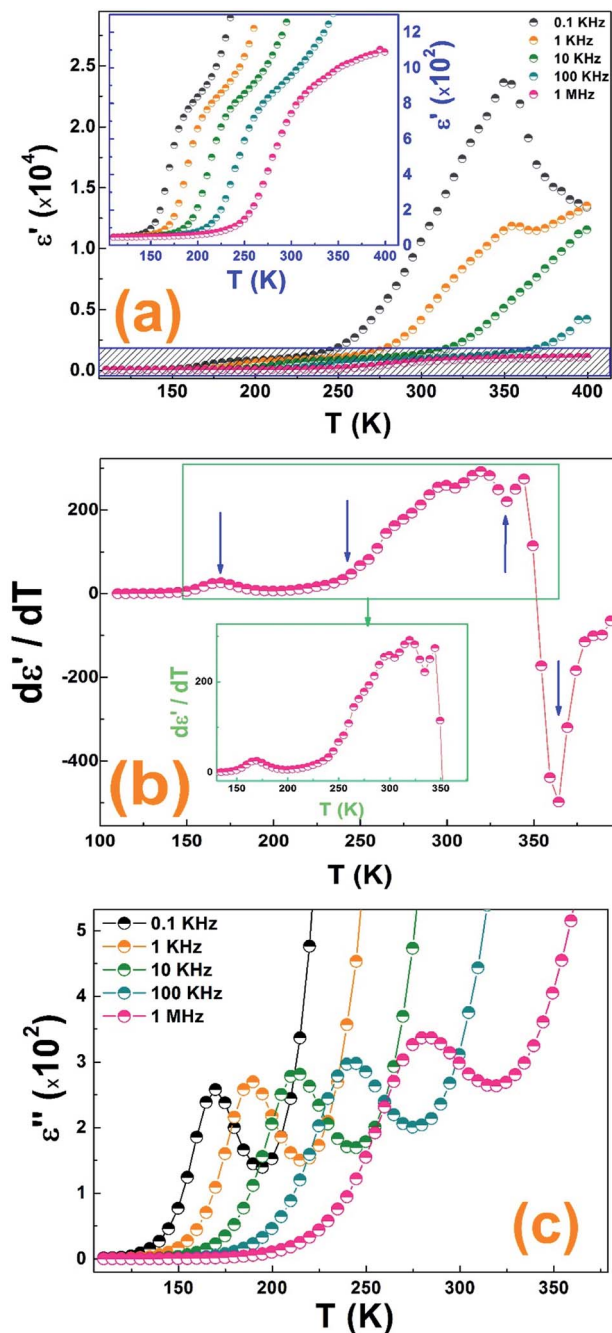
Fig. 5 Temperature dependence of (a) the real part of the dielectric permittivity (b) the derivation of the real part of the dielectric permittivity (c) the imaginary part of the dielectric permittivity.

studied compound under the same frequency range. This figure proves clearly the $(La_{0.8}Ca_{0.2})_{0.4}Bi_{0.6}FeO_3$ material reveals a relaxor ferroelectric behavior in the temperature range 180–240 K. Thus, we can assume that the detected transition at 240 K to 350 K in the $\varepsilon'$ temperature dependence spectra can identify a dielectric transition from ferroelectric to paraelectric state.

Indeed, the real dielectric permittivity start to increase at 240 K until reaching a maximum at around 350 K and then it starts to decrease sharply.

It is important to mention that the increase in frequency was accompanied by a rapid drop in the maximum dielectric constant at 350 K. This decrease results from the reduction of space charge polarization effect. Further, the achieved colossal dielectric constant at low frequency ($\approx 2.3 \times 10^4$) is attributed to the existence of a potential barrier generated by space charge polarization at the grain boundaries which induces a charge accumulation at the grain boundaries produced at higher $\varepsilon'$ values. Such high value, in the paraelectric phase, allows the use of this material in energy storage devices.[37] Thus, the dielectric dispersion can be understood according to the Koop's phenomenological theory based on Maxwell Wagner's interfacial polarization model estimating that a dielectric can be considered as an inhomogeneous medium containing two different layers, fairly well conducting grains separated by poorly conducting grain boundaries.

As a result, the temperature dependence of the permittivity spectra can estimate the dielectric behavior of the $(La_{0.8}\text{-}Ca_{0.2})_{0.4}Bi_{0.6}FeO_3$ material. Due to the diversity of the application field of the ferroelectric material, the investigation of the frequency dependence of dielectric behavior will be aimed to the ferroelectric phase of this material above the $T_c = 350$ K.

**3.4.2 Frequency dependence of dielectric behavior.** To correlate with the last section, we will devise the next study on three temperature regions: region I: 150–170 K, region II: 180–240 K and region III: 250–320 K.

Based on the Cole–Cole model, the experimental data of the real and imaginary parts of the dielectric permittivity can be analyzed based on the following expressions:[36]

$$\varepsilon'(\omega) = \varepsilon_\infty + \frac{(\varepsilon_s - \varepsilon_\infty) \times [1 + (\tau\omega)^\alpha \times \cos(\alpha\pi/2)]}{1 + (\tau\omega)^{2\alpha} + 2 \times (\tau\omega)^\alpha \times \cos(\alpha\pi/2)} \quad (2)$$

$$\varepsilon''(\omega) = \varepsilon_\infty + \frac{(\varepsilon_s - \varepsilon_\infty) \times (\tau\omega)^\alpha \times \sin(\alpha\pi/2)}{1 + (\tau\omega)^{2\alpha} + 2 \times (\tau\omega)^\alpha \times \cos(\alpha\pi/2)} \quad (3)$$

$\varepsilon_s$ and $\varepsilon_\infty$ are the values of the static dielectric constant determined at low and high frequency respectively. Also, $\tau$ is the relaxation time and $\alpha$ describes the distribution of relaxation times.

Fig. 6(a) shows the frequency dependence of the permittivity real part of the $(La_{0.8}Ca_{0.2})_{0.4}Bi_{0.6}FeO_3$ sample under the three cited temperature regions. These plots prove clearly only one Cole–Cole kind dispersion below 180 K (region I), at low frequencies, due to the interfacial polarization, that shift to the high frequencies. While in the region II, two Cole–Cole dispersions are visible where one appears from low frequencies region.

It is to note that, when increasing temperature, all dielectric dispersions shift to higher frequencies showing at the time the frequency and temperature dependence of the dielectric constant and that the polarization process gradually vanishes at high frequency range. Moreover, for all temperatures, it is clear that $\varepsilon'$ becomes frequency independent at the high applied frequencies suggesting that almost of diploes do not respond the applied frequency.
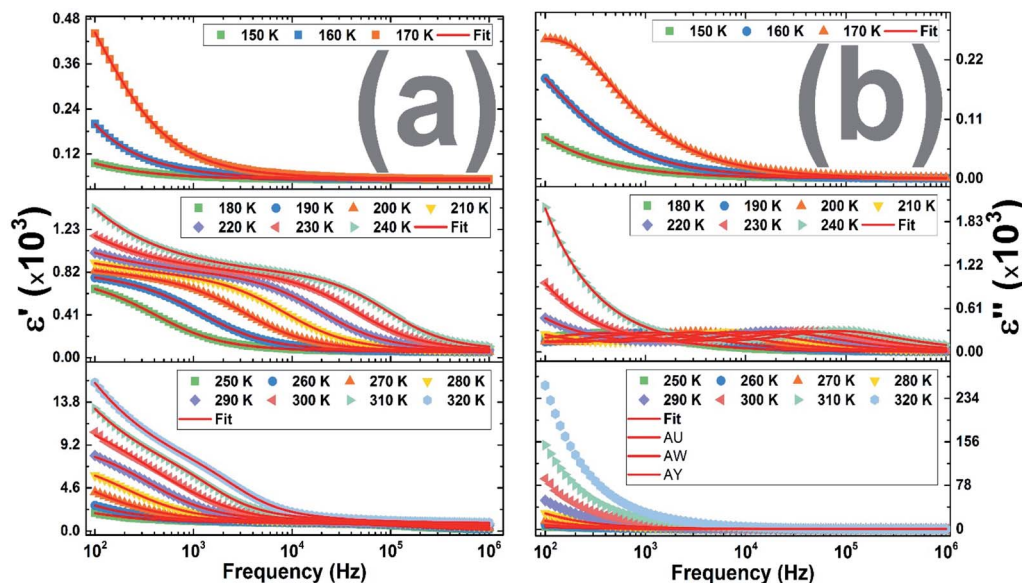
**Fig. 6** Frequency dependence of (a) the real part of the dielectric permittivity (b) the imaginary part of the dielectric permittivity.

These two processes are mainly attributed to the interfacial and dipolar polarizations[37] explaining the appearance of dielectric relaxations in the $\varepsilon''$ spectra as shown in Fig. 6(b).

Fig. 7(a) illustrates the variation of the imaginary complex modulus part of $(La_{0.8}Ca_{0.2})_{0.4}Bi_{0.6}FeO_3$ compound as a function of frequency in the three temperature regions. In region I and II, the plots show clearly the appearance of resolved peaks at unique frequency indicating a transition from long to short range mobility where the carriers are confined to potential wells. This peak translates to the high frequency region indicating a decrease in the relaxation time with increasing temperature and then its thermal activation.[38]

Another key point, this peak start to disappear and a new one appear from the low frequencies after 240 K. The coexisting of the two observed relaxation between 240 K and 320 K (region III) can be related to the long behavior of the observed dielectric transition.[39] As shown in Fig. 7(b), the variation of tg $\delta$ *versus* frequency, plots in the different temperature regions, follows the same behavior of $M''$. Further, we noted low values of dielectric loss that can mention the high quality of the $(La_{0.8}$-$Ca_{0.2})_{0.4}Bi_{0.6}FeO_3$ as material for energy storage devices.[40]

In Fig. 7(c), it is plotted the dependence of $Z''$ on frequency of the studied material at the three temperature regions. We clearly observe one peak starts to appear after 180 K (region II) while we note the appearance of a second one in the third temperature region affirming the presence of two different relaxation phenomena where it's are present two different structures.[41]

In another hand, the observed relaxation peaks, corresponding to the maximal values of $Z''$ curves, translate to the high frequency region as the temperature increases indicating the thermal activated behavior of the relaxation process. It is also important to mention that for each measuring temperature, the relaxation peaks shift to the higher frequencies proving a reduction of the relaxation.[42] Moreover, at higher

frequency region, we noted a merge of all the $Z''$ curves and any dependence on both frequency and temperature due to the space charge accumulation in the material where its do not require more time to relax at high frequencies leading to the reduction of their polarization with the frequency rising.[43]

To more understand this behavior of transition, we plotted in Fig. 8 the variation of $\log(f_{max})$ as a function of the $1000/T$, from the experimental data of the impedance, modulus and tg $\delta$, according to the Arrhenius law:

$$f_{max} = f_0 \exp\left(-\frac{E_a}{k_B T}\right) \qquad (4)$$

where

$f_{max}$ is the frequency corresponding to the maximum value of the imaginary part of the complex modulus $M''$.

$f_0$ is a pre-exponential factor.

$E_a$ is the activation energy.

$k_B$ is the Boltzmann constant.

$T$ is the temperature.

As clearly seen, Fig. 8 shows the existence of four linear regions, three regions with negative slopes corresponding to the FE and PE phases and one another region with a positive slope around 240 K corresponding to the FE–PE transition[39] which needs a time to pass from the FE phase to the PE[39] phase confirming then the above observed behavior.

**3.4.3 Frequency dependence of electrical behavior.** The variation of AC conductivity, $\sigma_{ac}$, with frequency under the three temperature regions is plotted in Fig. 9(a). This figure shows clearly that $\sigma_{ac}$ is frequency independent corresponding to a plateau type behavior at the low frequency region.

The frequency effect is appeared only at high frequencies, which is manifested of a dispersion behavior. Therefore, in this frequency region, the conductivity is provided with a second term deriving from the ionic atmosphere relaxation after particles movement and follows the universal power law of $(A\omega^s)$.[44]
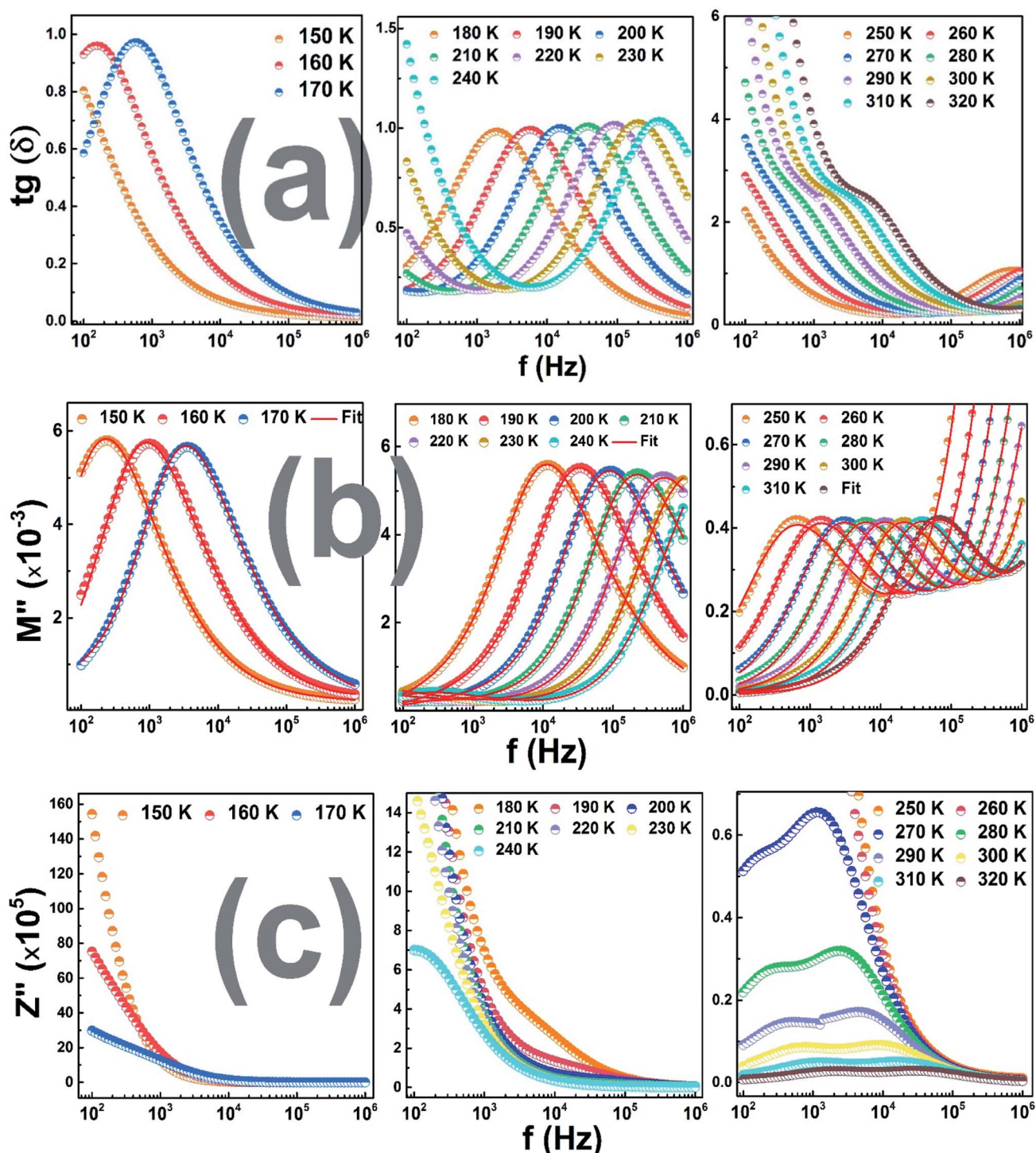
Fig. 7 Frequency dependence of (a) tg $\delta$, (b) the imaginary part of the electrical modulus, (c) the imaginary part of the impedance.

By respecting the temperature dependence of the dielectric properties discussed below, we can clearly observe the presence of only one dispersion behavior in region I of temperature. While a second one appeared in region II and starts to disappear after the first one after 240 K. This behavior proves that the conductivity enhancement results from the improvement of the hopping probability of charge carriers by the frequency increasing.

Accordingly, the relaxation appeared in the $\varepsilon'$ and $\sigma_{ac}$ variation *versus* frequency can be described by the combination juxtaposition of two behaviors corresponding to the observed ferroelectric to paraelectric transition near to the room temperature.

Therefore, according to the above discussion, the AC conductivity dispersion can be analyzed based on the following equation:[45]
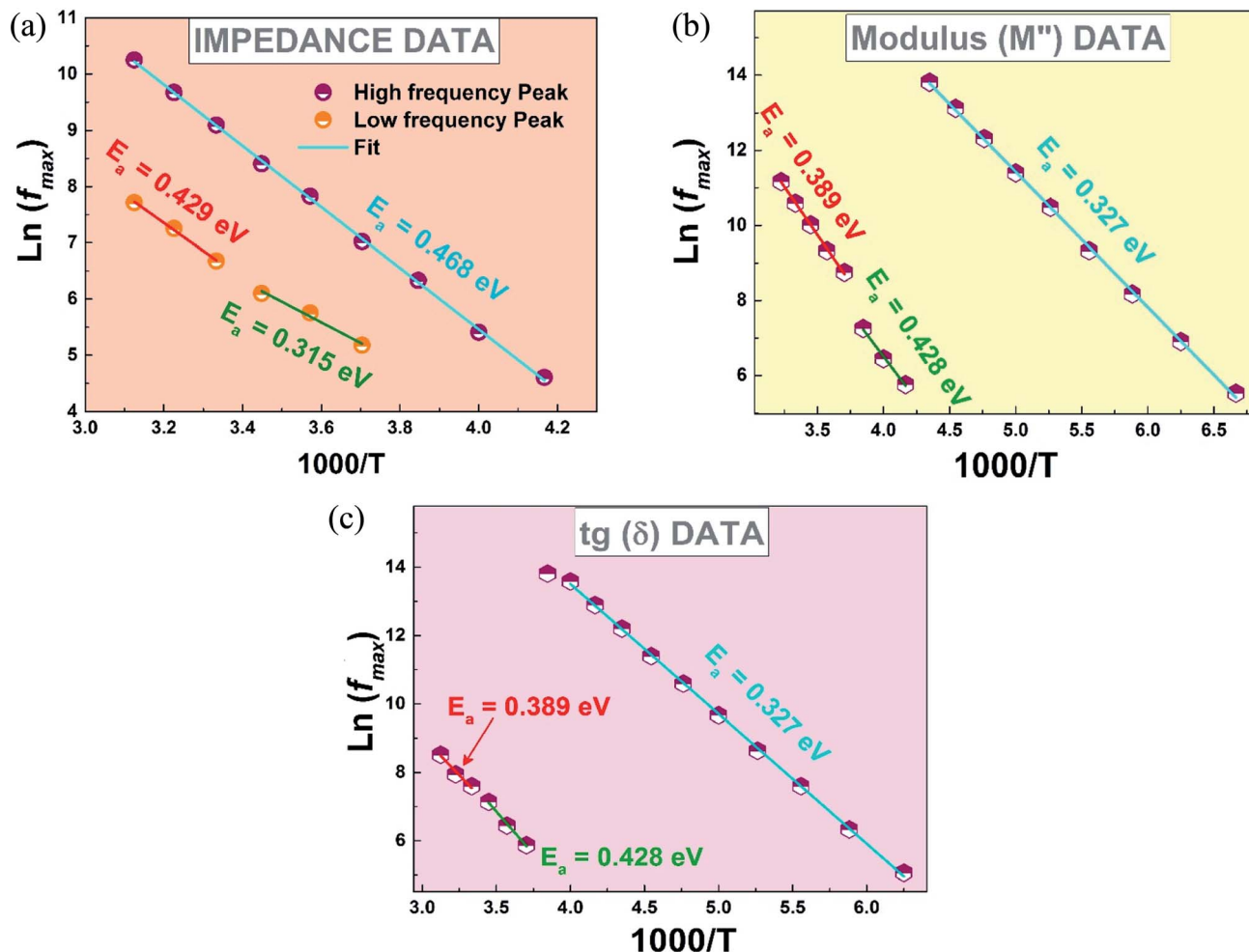
**Fig. 8** Variation of ln($f_{max}$) *versus* 1000/$T$ from (a) the impedance data (b) the modulus data (c) tg $\delta$ data.

$$\sigma_{ac}(\omega) = \left[ \frac{\sigma_s}{1 + \tau^2\omega^2} + \frac{\sigma_\infty \tau^2\omega^2}{1 + \tau^2\omega^2} \right] + A\omega^s \qquad (5)$$

where

$\sigma_s$ presents the conductivity at low frequencies, $\sigma_\infty$ is an estimate of conductivity at high frequencies, $\omega = 2\pi f$ refers to the angular frequency, $\tau$ corresponds to the characteristic relaxation time, $A$ is a temperature dependent constant that determines the strength of polarizability[46] and $s$ is the power law exponent describing the degree of interaction between mobile ions with the environments surrounding them.

The variation of DC conductivity, with the reciprocal temperature for this compound, is shown in Fig. 9(c).

In the different distinguished regions, this graph shows a linear response explained by a thermally activated transport having an Arrhenius type behavior which is expressed by the following law:

$$\sigma_{dc} = \sigma_0 \exp\left( -\frac{E_a}{k_B T} \right) \qquad (6)$$

where: $\sigma_0$ denotes the DC conductivity pre-exponent factor, $E_a$ presents the activation energy of the mobile charge carriers.

The observed plots exhibited the same behavior as the observed one in Fig. 8 confirming once again the dielectric phase transition between 240 K and 350 K with a the decrease in the activation energies values in the three regions. Once can see that the conductivity increases with the increase of temperature while the activation energy has the same behavior *i.e.*, $E_a$ increase with increasing temperature, which is in good agreement with the fact that lower activation energy is associated with higher dielectric constant and higher conductivity.[47]

Furthermore, the variation of "$s$" with temperature is shown in Fig. 9(c). The behavior of this exponent with respect to temperature is a powerful indicator of the origin of the conduction mechanism. It is noted that, for the studied material, this behavior varies remarkably with the considered temperature range.

Indeed, in region I, a decrease in the exponent $s$ with the increase in temperature is observed due to the increase in the interaction. In region II, two exponent, $s_1$ and $s_2$ are observed corresponding to the observed dispersion in the ac conductivity spectra in this region of temperature. The minimum reached at 240 K implies the strong interaction between the charge carriers
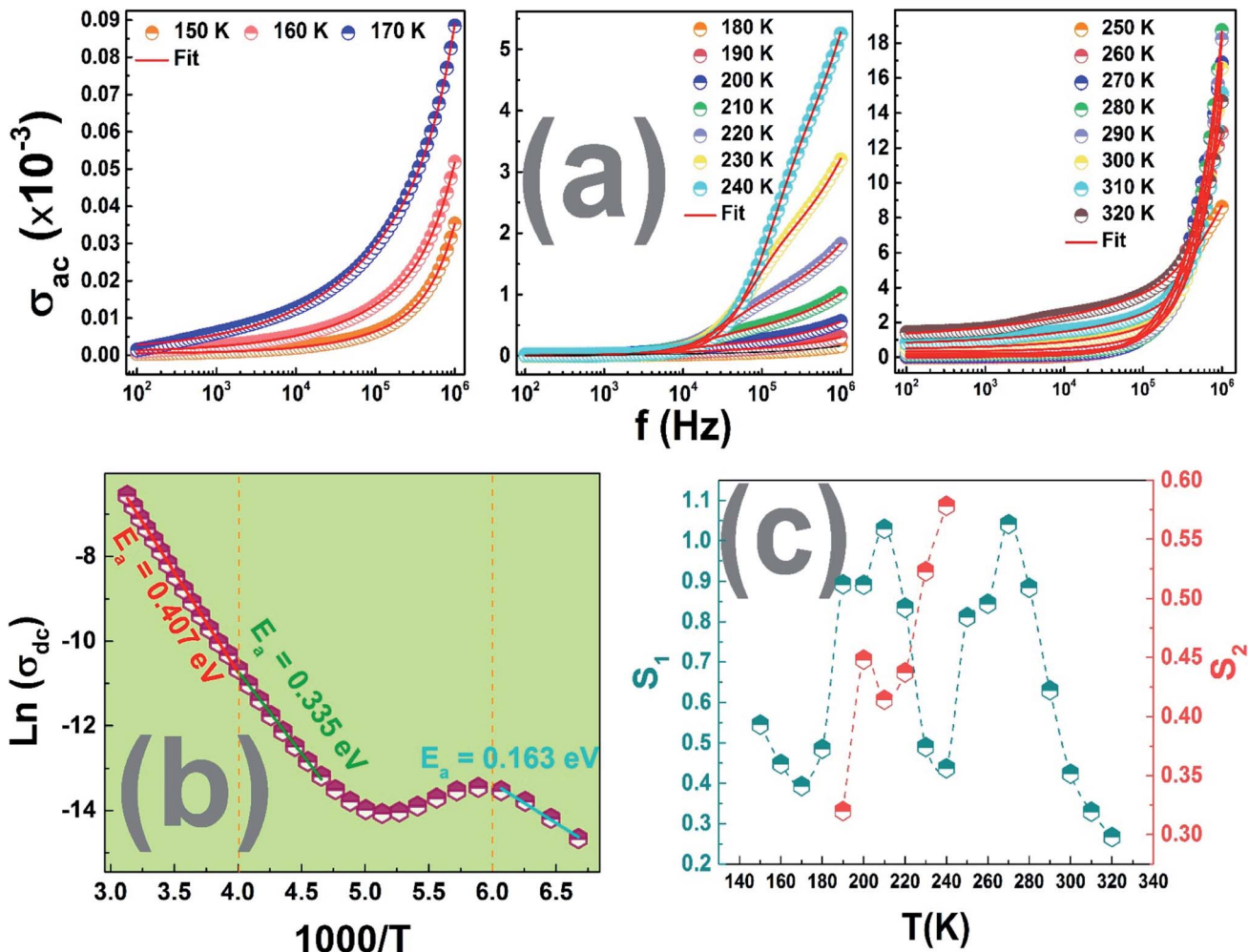
Fig. 9 (a) Frequency dependence of de ac conductivity at the three temperature regions (b) variation of $\ln(f_{max})$ *versus* 1000/$T$ from ac conductivity data (c) variation of the exponent $s$ *versus* temperature.

and the lattices. Such behavior proves the predominance of the correlated barrier hopping (CBH) conduction mechanism.

Then, in region III an increase in the exponent $s$ with the increase in temperature is observed indicating a small polaron tunnel (NSPT). After that, a decreasing of $s$ beckons an increase in the randomness in the system. In fact, for high temperatures, dipoles and charge carriers respond independently to the external field. Therefore, the conduction model which is often adopted for such behavior is the CBH one.

## 4. Conclusion

$(La_{0.8}Ca_{0.2})_{0.4}Bi_{0.6}FeO_3$ nanoparticles, synthesized by means of sol–gel process, were found to have a perovskite-type structure with the coexistence of $R3c$ and $Pnma$ space groups at room temperature. TEM observation proves the formation of spherical and polygonal nanoparticles. By conducting comprehensive dielectric and electrical studies on the prepared material, an anomaly in the dielectric constant was detected near the room temperature, corresponding to a typical FE–PE transition with a colossal value of real permittivity at 350 K that allows the use

of this material in energy storage devices. This anomaly is well confirmed by supplementary analyzes of the complex electrical modulus and the AC conductivity spectra. On the other hand, the correlated barrier hopping (CBH) conduction mechanism was proven to be dominant in the temperature ranges of 150–170 K, the two observed exponent, $s_1$ and $s_2$ between 180 K and 270 K correspond to the observed dispersions in the ac conductivity spectra in this region of temperature, unlike the temperature range of 240 K at 320 K where the small polaron tunnel (NSPT) was considered the appropriate conduction model.

## Conflicts of interest

There are no conflicts to declare.

## Acknowledgements

# References

1 I. C. Nlebedim, M. Vinitha, P. J. Praveen, D. Das and D. C. Jiles, *J. Appl. Phys.*, 2013, **113**, 193904.

2 A. Benali, S. Azizi, M. Bejar, E. Dhahri and M. F. P. Graça, *Ceram. Int.*, 2014, **40**, 14367.

3 K. T. C. Roseno, R. Brackmann, M. A. da Silva and M. Schmal, *Int. J. Hydrogen Energy*, 2016, **41**, 18178.

4 S. J. Skinner, *Fuel Cell. Bull.*, 2001, **4**, 6–12.

5 E. Delgado and C. R. Michel, *Mater. Lett.*, 2006, **60**, 1613–1616.

6 V. S. Kolat, H. Gencer, M. Gunes and S. Atalay, *Mater. Sci. Eng. B*, 2007, **140**, 217.

7 A. S. Mahapatra, A. Mitra, A. Mallick, A. Shaw, J. M. Greneche and P. K. Chakrabarti, Modulation of magnetic and dielectric property of LaFeO3 by simultaneous doping with Ca2+ and Co2+-ions, *J. Alloys Compd.*, 2018, **743**, 274–282.

8 P. Barahona, O. Peña, A. B. Antunes, C. Campos, G. Pecchi, Y. Moreno, C. Moure and V. Gil, *J. Magn. Magn. Mater.*, 2008, **320**, 61–64.

9 A. Bougoffa, A. Benali, M. Bejar, E. Dhahri, M. P. F. Graca, M. A. Valente, L. Bessais and B. F. O. Costa, *J. Alloys Compd.*, 2021, **856**, 157425.

10 A. Benali, M. Bejar, E. Dhahri, M. P. F. Graça, M. A. Valente, E. K. Hlil and B. F. O. Costa, Structural, dielectric relaxation and magnetic features of the (La0.8Ca0.2)0.9Bi0.1Fe1−yTiyO3 (y = 0.0 and 0.1) nanoparticles, *J. Alloys Compd.*, 2021, **876**, 160222.

11 E. M. Benali, A. Benali, M. Bejar, E. Dhahri, M. P. F. Graca, M. A. Valente and B. F. O. Costa, Effect of synthesis route on structural, morphological, Raman, dielectric, and electric properties of La0.8Ba0.1Bi0.1FeO3, *J. Mater. Sci.: Mater. Electron.*, 2020, **31**, 3197–3214, DOI: 10.1007/s10854-020-02867-0.

12 E. M. Benali, A. Benali, M. Bejar, E. Dhahri, M. P. F. Graca, M. A. Valente, P. Sanguino and B. F. O. Costa, Effect of annealing temperature on structural, morphological and dielectric properties of La$_{0.8}$Ba$_{0.1}$Ce$_{0.1}$FeO$_3$ perovskite, *J. Mater. Sci.: Mater. Electron.*, 2020, **31**, 16220–16234.

13 M. Coskun, F. M. Coskun, Z. Durmus, M. Caglar and A. Turut, Os doped YMnO3 multiferroic: A study investigating the electrical properties through tuning the doping level, *J. Alloys Compd.*, 2018, **752**, 274–288.

14 P. R. Ren, Z. Liu, X. Wang, Z. Duan, Y. Wan, F. Yan and G. Zhao, Dielectric and energy storage properties of SrTiO3 and SrZrO3 modified Bi0.5Na0.5TiO3–Sr0.8Bi0.1□0.1TiO3 based ceramics, *J. Alloys Compd.*, 2018, **742**, 683–689.

15 B. Jaffe, Antiferroelectric ceramics with field-enforced transitions: a new nonlinear circuit element, *Proc. IRE*, 1961, **49**, 1264–1267.

16 A. Benali, B. M. G. Melo, P. R. Prezas, M. Bejar, E. Dhahri, M. A. Valente, M. P. F. Graça, B. A. Nogueira and B. F. O. Costa, Structural, morphological, Raman and ac electrical properties of the multiferroic sol–gel made Bi$_{0.8}$Er$_{0.1}$Ba$_{0.1}$Fe$_{0.96}$Cr$_{0.02}$Co$_{0.02}$O$_3$ material, *J. Alloys Compd.*, 2019, **775**, 304–315.

17 A. Benali, M. Bejar, E. Dhahri, M. F. P. Graça and L. C. Costa, Electrical conductivity and ac dielectric properties of La0.8Ca0.2−xPbxFeO3 (x = 0.05, 0.10 and 0.15) perovskite compounds, *J. Alloys Compd.*, 2015, **653**, 506–512.

18 R. A. Young, *The Rietveld Method*, Oxford University Press, New York, 1993.

19 M. M. Costa, G. F. M. Pires Junior and A. S. B. Sombra, Dielectric and impedance properties' studies of the of lead doped (PbO)-Co$_2$Y type hexaferrite (Ba$_2$Co$_2$Fe$_{12}$O$_{22}$(Co$_2$Y)), *Mater. Chem. Phys.*, 2010, **123**, 35.

20 M. P. F. Graça, M. G. F. da Silva and M. A. Valente, NaNbO$_3$ crystals dispersed in a B$_2$O$_3$ glass matrix–Structural characteristics *versus* electrical and dielectrical properties, *Solid State Sci.*, 2009, **11**, 570–577.

21 E. V. Ramana, F. Figueiras, A. Mahajan, D. M. Tobaldi, B. F. O. Costa, M. P. F. Graça and M. A. Valente, Effect of Fe-doping on the structure and magnetoelectric properties of (Ba0.85Ca0.15)(Ti0.9Zr0.1)O3 synthesized by a chemical route, *J. Mater. Chem. C*, 2016, **4**, 1066–1079.

22 L. Sangaletti, L. E. Depero, B. Allieri, P. Nunziante and E. Traversa, An X-ray study of the trimetallic LaxSm1−xFeO3 orthoferrites, *J. Eur. Ceram. Soc.*, 2001, **21**, 719–726.

23 A. Benali, A. Souissi, M. Bejar, E. Dhahri, M. F. P. Graca and M. A. Valente, Dielectric properties and alternating current conductivity of sol–gel made La$_{0.8}$Ca$_{0.2}$FeO$_3$ compound, *Chem. Phys. Lett.*, 2015, **637**, 7.

24 A. K. Ghosh, G. D. Dwivedi, B. Chatterjee, B. Rana, A. Barman, S. Chatterjee and H. D. Yang, *Solid State Commun.*, 2013, **166**, 22.

25 P. Kharel, S. Talebi, B. Ramachandran, A. Dixit, V. M. Naik, M. B. Sahana, C. Sudakar, R. Naik, M. S. R. Rao and G. Lawes, Structural, magnetic, and electrical studies on polycrystalline transition-metal-doped BiFeO3 thin films, *J. Phys.: Condens. Matter*, 2009, **21**, 036001.

26 W. Y. Xing, Y. N. N. Ma, Y. L. Bai, S. F. Zhao, *et al.*, Enhanced ferromagnetism of Er-doped BiFeO3 thin films derived from rhombohedral-to-orthorhombic phase transformations, *Mater. Lett.*, 2015, **161**, 216–219.

27 L. Peng, H. M. Deng, J. J. Tian, Q. Ren, C. Penga, Z. P. Huang, P. X. Yanga and J. H. Chu, Influence of Co doping on structural, optical and magnetic properties of BiFeO3 films deposited on quartz substrates by sol–gel method, *Appl. Surf. Sci.*, 2013, **268**, 146–150.

28 N. S. Goncalves, J. A. Carvalho, Z. M. Lima and J. M. Sasaki, *Mater. Lett.*, 2012, **72**, 36.

29 A. V. Naumkin, A. K. Vass, S. W. Gaarenstroom and C. J. Powell, *NIST X-ray Photoelectron Spectroscopy Database, NIST Standard Reference Database 20*, version 4.1, see https://srdata.nist.gov/xps/.

30 Y. Zhang, Y. Wang, J. Qi, Y. Tian, M. Sun, J. Zhang, T. Hu, M. Wei, Y. Liu and J. Yang, Enhanced Magnetic Properties of BiFeO$_3$ Thin Films by Doping: Analysis of Structure and Morphology, *Nanomaterials*, 2018, **8**, 711.

31 X. Li, H. B. Zhang, X. X. Liu, S. Li and M. Zhao, XPS study on O(1s) and Fe(2p) for nanocrystalline composite oxide LaFeO$_3$ with the perovskite structure, *Mater. Chem. Phys.*, 1994, **38**, 355–362.

32 M. Kamali, M. E. V. Costa, G. Otero-Irurueta and I. Capela, Ultrasonic irradiation as a green production route for coupling crystallinity and high specific surface area in iron nanomaterials, *J. Cleaner Prod.*, 2019, **211**, 185–197.

33 R. Singh, P. K. Gupta, S. Kumar, A. G. Joshi, A. K. Ghosh, S. Patil and S. Chatterjee, Enhancement in electrical and magnetic properties with Ti-doping in Bi$_{0.5}$La$_{0.5}$Fe$_{0.5}$Mn$_{0.5}$O$_3$, *J. Appl. Phys.*, 2017, **121**, 154101.

34 A. R. Rajamani, S. Jothi, M. D. Kumar, S. Srikaanth, M. K. Singh, G. Otero-Irurueta, D. Ramasamy, M. Datta and M. Rangarajan, Effects of Additives on Kinetics, Morphologies and Lead-Sensing Property of Electrodeposited Bismuth Films, *J. Phys. Chem. C*, 2016, **120**, 22398–22406.

35 F. Akram, J. Kim, S. A. Khan, A. Zeb, H. G. Yeo, Y. S. Sung, T. K. Song and M.-H. Kim, Soonil Lee Less temperature-dependent high dielectric and energy-storage properties of ecofriendly BiFeO3–BaTiO3-based ceramics, *J. Alloys Compd.*, 2020, **818**, 152878.

36 W. Ncib, A. Ben Jazia Kharrat, M. A. Wederni, N. Chniba-Boudjada, K. Khirouni and W. Boujelben, Investigation of structural, electrical and dielectric properties of sol–gel prepared La$_{0.67-x}$Eu$_x$Ba$_{0.33}$Mn$_{0.85}$Fe$_{0.15}$O$_3$ (x = 0.0, 0.1) manganites, *J. Alloys Compd.*, 2018, **768**, 249–262.

37 I. Bunget and M. Popescu, *Physics of solid dielectrics*, Elsevier, Amsterdam, Oxford, New York, Tokyo, 1984.

38 N. Kumar, A. Dutta, S. Prasad and T. P. Sinha, Dielectric relaxation of complex perovskite Sm(Ni1/2Zr1/2)O3, *Physica B*, 2010, **405**, 4413–4417.

39 I. Coondoo, N. Panwar, R. Vidyasagar and A. L. Kholkin, *Phys. Chem. Chem. Phys.*, 2016, **18**, 31184–31201.

40 P. R. Mandal, S. Sahu and T. K. Nath, *Int. J. Nanosci.*, 2011, **10**, 295.

41 S. Hcini, A. Selmi, H. Rahmouni, A. Omri and M. L. Bouazizi, *Ceram. Int.*, 2017, **43**, 2529.

42 C. Bharti and T. P. Sinha, *Physica B*, 2011, **406**, 1827–1832.

43 S. Nasri, A. L. Ben Hafsia, M. Tabellout and M. Megdiche, *RSC Adv.*, 2016, **6**, 76659.

44 A. K. Jonscher, *Universal Relaxation Law*, Chelsea Dielectric Press, London, 1996.

45 M. Dussouze, Second harmonic generation in glasses borophosphate sodium and niobium thermal polarization, thesis, University Bordeaux I, France, 2005.

46 W. H. Jung, *Physica B*, 2001, **299**, 120.

47 J. Smith and H. B. J. Wign, *Ferrites*, Cleaver-Hume Press, London, 1959.